PHYSICAL SCIENCES

Flow-induced "waltzing" red blood cells: Microstructural reorganization and the corresponding rheological response

Chih-Tang Liao[1,2,3]†, An-Jun Liu[1,4,5]†, Yeng-Long Chen[1,6,7]*

We investigate flow-induced structural organization in a dilute suspension of tumbling red blood cells (RBCs) under confined shear flow. For small Reynolds ($Re = 0.1$) and capillary numbers (Ca), with fully coupled hydrodynamic interaction (HI) and without interparticle adhesion, we find that HI between the biconcave discoid particles prompts the formation of layered RBC chains and synchronized rotating RBC pairs, referred here as "waltzing doublets." As the volume fraction ϕ increases, more waltzing doublets appear in RBC files. Stronger shear stress disrupts structural arrangements at higher Ca. We find that the flow-induced organization of waltzing doublets changes how the suspension viscosity varies with ϕ qualitatively. The intrinsic viscosity is particularly sensitive to microstructural rearrangement, increasing (decreasing) with ϕ at low (high) Ca that correlates with the change in the fraction of doublets. We verified flow-induced collective motion with comparison to two-cell simulations in which the cell volume fraction is controlled by varying the domain volume.

INTRODUCTION

Intriguing microstructures and phase transitions can emerge in equilibrium colloidal suspensions depending on thermal fluctuations, the volume fraction of dispersed substances, and interparticle interaction (*1*, *2*). The presence of external fields, such as a thermal, an electromagnetic, or a flow field could also give rise to the emergence of nonequilibrium collective motion and dynamic patterns (*3*, *4*). In both passive and active particle suspensions, long-range hydrodynamic interaction yields captivating correlated particle motion (*5*–*9*). Spatial confinement modulates interparticle interaction and introduces near boundary hydrodynamic effects. Thus, it plays a crucial role in inducing ordered microstructures (*10*–*12*). Shear-induced transition from a disordered to an ordered microstructure could account for remarkable changes in suspension rheology (*11*, *13*). Consequently, the rheological characteristics of a particular suspension depend on the particle volume fraction, shear rate, and confinement length, among other factors.

Because of the physiological importance of red blood cells (RBCs), the microstructure and dynamics of RBC suspensions have been extensively studied. Understanding the flow dynamics of artificial capsules, RBCs, and other biological cells enables single particle manipulation and collective assembly for biomedical engineering and physiological diagnostics and treatments (*14*, *15*). Studies have illustrated that blood and blood cell properties can serve as indicators for pathological conditions (*16*, *17*), and soft polymeric microcapsules have applications as molecular drug carriers (*18*). Furthermore, intercellular attraction induces RBC aggregation and severely affects blood viscosity response to shear flow (*19*–*21*). RBC clustering can cause both shear thickening and shear thinning in blood flow (*22*, *23*), which could indicate abnormally increased concentrations of attraction-inducing molecules in the blood (*20*, *24*).

The RBC can be viewed as a bag of cytoplasm composed of a lipid bilayer supported on a spectrin network. Despite its relatively simple cell structure, it exhibits complex viscoelastic dynamics. In shear flow, RBCs manifest various cell shapes with different modes of motion such as tumbling, rolling, and tank-treading governed by the shear rate, RBC elasticity, spatial confinement, and inner/outer fluid viscosity contrast (*25*).

A recent rheoscope experiment shows that files of regularly spaced RBCs along the flow direction can develop in unidirectional shear flow (*7*), and accompanying numerical simulations suggest that other simple crystalline arrangements are also possible (*7*). A two-dimensional (2D) numerical simulation reveals that, in addition to the single file arrangement, RBCs can reorganize as two stacked files along the shear gradient direction as the volume fraction increases, with cells passing each other. Moreover, files of RBC doublets form under strong spatial constraints at high-volume fractions (*26*, *27*).

Under pressure-driven flow, parachute-shaped RBCs rearrange as a single file in a circular tube of a diameter less than 10 μm. As the hematocrit rises, RBCs would deform with slipper-like shapes and arrange in a zig-zag configuration. However, disordered arrangement prevails in wider tubes (*28*). Similarly, in a quasi-2D rectangular microfluidic channel, either single or multiple files of RBCs can emerge, depending on the hematocrit, the channel width, and the magnitude of pressure drop. Stiffer membrane elasticity, nevertheless, hinders the formation of ordered configurations (*6*, *7*).

The key physical forces that influence hydrodynamics-driven particle motion in flow are particle inertia, viscous dissipation, and particle elasticity. The particle Reynolds number $Re_p \equiv \rho\dot{\gamma}R^2/\eta$ captures the effects of particle inertia relative to viscous dissipation, and the capillary number $Ca \equiv \eta\dot{\gamma}R/G$ indicates the ratio of the fluid stress to the particle elastic restoring stress. Here, ρ is the fluid density, $\dot{\gamma}$ is the shear rate, R is the RBC radius, η is the fluid viscosity, and G denotes the RBC shear modulus. In dilute microparticle suspensions,

[1]Institute of Physics, Academia Sinica, Taipei 11529, Taiwan (R.O.C.). [2]Department of Engineering and System Science, National Tsing Hua University, Hsinchu 30004, Taiwan (R.O.C.). [3]Nano Science and Technology Program, Taiwan International Graduate Program, Academia Sinica and National Tsing Hua University, Taipei 11529, Taiwan (R.O.C.). [4]Department of Physics, National Taiwan University, Taipei 10621, Taiwan (R.O.C.). [5]Department of Physics, University of Illinois at Urbana-Champaign, Urbana, IL 61801, USA. [6]Department of Chemical Engineering, National Tsing Hua University, Hsinchu 30004, Taiwan (R.O.C.). [7]Physics Division, National Center for Theoretical Sciences, Taipei 10621, Taiwan (R.O.C.).
*Corresponding author. Email: yenglong@phys.sinica.edu.tw
†These authors contributed equally to this work.

hydrodynamic interactions between the particles and the wall boundaries dominate the physical mechanisms of hydrodynamics-driven cross-stream particle migration, which has been well characterized and understood in the regime of $Re_p \ll 1$ and $Ca \ll 1$ (*29*–*40*). In dense suspensions of soft particles, the interplay between particle cross-stream migration and interparticle collisions results in particle-free layers that can substantially affect suspension rheology (*22*, *23*, *41*). In this study, we keep Re_p constant at 0.1 and allow Ca to vary between 0.01 and 0.2.

Limited analyses and modeling have suggested that interparticle hydrodynamic fields lead to collective microstructural reorganization in similar systems for tank-treading deformable particles (*7*, *8*). Here, we apply the lattice Boltzmann method coupled with model elastic biconcave capsules through the immersed boundary method (*42*) to investigate flow-driven microstructural rearrangements and the rheological consequences for tumbling RBC suspensions, without inter-RBC adhesion, under confined shear flow. We model the cell membrane as a discrete elastic spring network composed of 642 vertices and 1240 triangular faces. The fluid lattice grid size is $\Delta x = 0.5$ μm. RBCs are confined in a box domain $(L_x, L_y, L_z) \cong (18R, 3R, 18R)$ of volume $V = L_x L_y L_z$, with the RBC radius $R = 3.91$ μm. Two parallel walls at 0 and L_y move in opposite directions to induce shear flow in the x direction. The boundary condition along the x and z directions is periodic. For simplicity, the viscosity ratio of the RBC cytosol to the surrounding fluid is set to be unity. We focus on the dilute limit with the RBC volume fraction $0.02 < \phi = NV_{RBC}/V < 0.1$, where N is the total number of RBCs, and $V_{RBC} = 93.30\ \mu m^3$, in which the interparticle and near boundary hydrodynamic interactions both strongly influence single and collective particle dynamics. Each simulation trajectory length is longer than 2000 strains ($\gamma = \dot{\gamma}t$) such that the measured fluid stress reaches steady values. The model system corresponds to the dimensions of microvessels and microfluidic devices for biological and artificial cell sorting (*7*, *43*). The model schematics are shown in Fig. 1 (A and B), and additional details are given in Methods.

To compare how interparticle collective structure affects doublet formation and suspension rheology, we also perform simulations with only two RBCs in a chosen periodic domain matching the suspension volume fraction for comparison. In the two-cell model, the volume fraction is controlled by changing L_x and L_z. We place two RBCs at the center with an interparticle distance of 3 μm, and we generate an ensemble of 18 initial configurations for each set of ϕ and Ca by rotating the RBC pair about the z axis by $\Delta\theta = 10°$ and $\theta = [0, 180)$.

RESULTS

Waltzing RBCs

We identify three types of hydrodynamics-induced microstructural reorganization as shown in the top-down time-lapse snapshots in Fig. 1B and movies S1 to S3. For $Ca < 0.03$, a few RBC doublets form, turn synchronously for several rotations ("waltz"), and break apart intermittently. For $0.03 < Ca < 0.1$, the cells migrate toward the center flow plane because of cross-stream migration caused by near-wall hydrodynamic stress of a deformed elastic particle. In addition, the long-range interparticle hydrodynamic interaction reorganizes rotating RBCs in regularly spaced arrangements in the center flow plane, with zero average translational velocity. Correspondingly, the waltzing doublets synchronously rotate persistently for many cycles. For $Ca > 0.1$, RBC doublets are again more short-lived as the stronger shear forces pull pairs apart. However, the regularly spaced files of RBCs in the flow-vorticity (xz) plane remain, and the file width widens as RBCs flow past each other.

To quantify the aforementioned microstructures, we compute the 2D pair correlation function $g(r)$ by projecting the center-of-mass position of RBCs in the flow-vorticity (xz) plane. The peaks in $g(r)$ reflect the doublet formation, regularly spaced intrafile ordering along the flow direction and interfile ordering in the vorticity direction. For $r < 2R$, we observe peaks in $g(r)$ that indicate doublets as shown in Fig. 1 (C to E). For $Ca = 0.01$, a single peak appears for $r < 2R$, indicating doublets with regular spacing between paired RBCs. Two peaks emerge in the same region for $Ca = 0.07$, indicating that the inter-RBC spacing in doublets varies slightly during rotation at higher shear rates. In addition, RBCs form doublets and line up in files rather than assemble into disordered aggregates as depicted in the right and left insets of Fig. 1E, respectively. For $Ca = 0.18$, doublets are very short-lived as the RBCs move past others because of the stronger shear forces, and the peaks for $r < 2R$ disappear.

Figure 1 (C and D) shows that a lower cell volume fraction ($\phi < 5\%$) facilitates the formation of files of RBCs along the flow (x) direction, which is indicated by peaks in $g(r)$ for $r > 2R$. The peaks between $3R \leq r < 4R$ indicate the center-to-center distance between two neighboring cells in the same file, which may be bimodal, as shown in fig. S1. We find no simple dependence of the center-to-center distance between two neighboring synchronously rotating RBCs on the shear rate. Figure 1C shows that the peaks in $g(r)$ for $r \approx 6R$, $7R$, and $9R$, also shown in the snapshots in figs. S1 and S2, further indicate the long-range RBC file organization at a low ϕ.

The number of doublets should correlate with the average number of nearest neighbors, defined by $N_n = \int_0^l 2\pi r \phi g(r) dr$, where the upper limit l is chosen to be $1.53R$ near the location of the minimum of $g(r)$ for lower Ca (see Fig. 1, C to E). Figure 1F shows that N_n increases as Ca increases up to $Ca = 0.1$, followed by decreasing N_n as Ca further increases for all ϕ examined here.

Dynamics analysis

RBCs rotate/tumble in shear flow at low shear stresses (*44*, *45*). The rotation time t_{rot} of a single RBC in simple shear flow is the inverse of the rotation frequency, which varies linearly with the shear rate (*46*). We apply fast Fourier transform to a time series window of selected material points on each particle, as shown in fig. S3, to calculate the corresponding frequency spectrum and the rotation period.

We focus on the low Ca regime where the RBCs tumble or perform kayaking-like motion, in which the axis of revolution of the RBC precesses about the vorticity (z) axis (*47*). These solid-like motions resemble Jeffery orbits (*48*) that capture the motions of axisymmetric rigid particles under simple shear flow in the Stokes flow limit. We use the following criteria to quantify doublets: The time trajectory of the center-to-center distance between an RBC pair oscillates as the pair rotates. During an oscillation cycle, if the average distance is less than $2R$ and the maximum center-to-center distance is less than $8R/3$, then that pair of RBCs is counted as a doublet during that cycle. Movies S4 to S6 show waltzing RBC doublets identified through the above criteria. By checking these criteria along the time trajectory for all pairs of RBCs, we can identify the number of waltzing doublets $N_d(t)$ of a system at each time step and define the doublet fraction as $\Phi(t) = 2N_d(t)/N$.

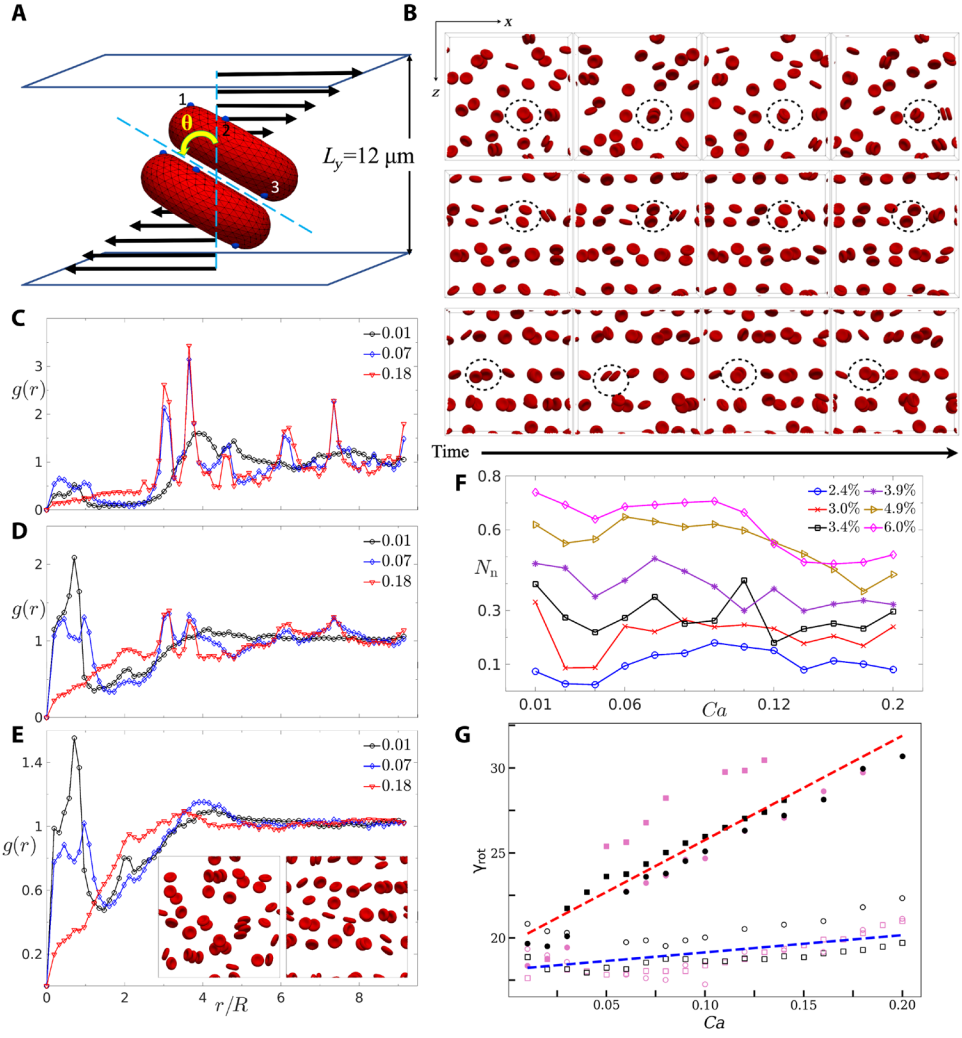

Fig. 1. RBC confined suspension structure and dynamics. (**A**) Schematic of the two-cell simulation, with the selected material points indicated by numbers. (**B**) Top-down view of time-lapse sequence snapshots of dilute RBC suspension in confined shear flow with $\phi = 0.045$ for $Ca = 0.01$ (top), 0.08 (middle), and 0.12 (bottom). The selected doublets in dashed circles illustrate the synchronized rotation as time progresses for each state. The *xz*-projected pair correlation function $g(r)$ for $\phi = 0.024$ (**C**), 0.04 (**D**), and 0.06 (**E**) at $Ca = 0.01$ (black circle), 0.07 (blue diamond), and 0.18 (red triangle). The insets in (E) show disordered RBCs (left) and aligned RBC aggregates (right) with $\phi = 0.06$ at $Ca = 0.01$ (left) and $Ca = 0.07$ (right). (**F**) The average number of the nearest neighbors dependence on Ca for various ϕ. (**G**) The averaged rotation times of doublets (filled symbols) and singlets (hollow symbols) dependence on Ca in the suspension (circles) and the two-cell (squares) system for $\phi = 0.04$ (pink) and 0.06 (black). The red and blue dashed lines are the linear regression fits.

To determine the rotation period $\gamma_{rot} = \dot{\gamma} t_{rot}$ of RBC doublets and singlets (in terms of strains), we first determine whether an RBC is in the doublet state at any given time. If an RBC is in the doublet state for longer than 90% of the time within a time window longer than 100 strains, then this time window is assigned as doublet dominant. Conversely, if an RBC is in the doublet state for shorter than 10% of the time within a time window longer than 100 strains, then this time window is assigned as singlet dominant. Within these windows, we calculate γ_{rot} for each RBC. We calculate the average rotation period of a given state (Ca, ϕ) from the average of the rotation periods for all RBCs in all ensembles corresponding to the state.

For both the suspension and the two-cell system, the doublet rotation period increases linearly from about 20γ to about 30γ as Ca increases from 0.01 to 0.2, while the singlet rotation period varies within 10% of 20γ (Fig. 1G). For the singlet RBCs in the suspension and in the two-cell system, γ_{rot} is nearly independent of Ca. The onset of particle rotation at small Ca also appears consistent with previous reported results (*46*, *49*). In contrast, the doublet rotation period increases as Ca increases with a slope ≈ 60 in both the suspension and the two-cell system, indicating increased resistance compared to the singlet. This may be attributed to the increased effective hydrodynamic radius of the doublet leading to increased friction. The effective hydrodynamic radius may increase with the shear rate due to increased separation within the doublet as a result of increased shear stress.

To further analyze the RBC motion, we determine the RBC rolling angle Ψ [defined by the angle between the vorticity (z) axis and the normal vector at the biconcave dimple] and the tumbling angle θ [defined by the angle between the flow (x) direction and the projection of the major axis of the deformed RBCs on the xy plane]. Note S1 and figs. S3 and S4 provide examples of the detailed rotation

analysis. The ensemble average of these two angles is defined as the average over all particles in all trials for chosen ϕ and *Ca*, over the last quarter period of the simulation. The average rolling angle $\langle\Psi\rangle = 0.29 \pm 0.01\ \pi$ at $\phi = 2\%$ and saturates at $0.37 \pm 0.01\ \pi$ at $\phi = 6\%$, and it is largely independent of *Ca* with $Re_p = 0.1$. The averaged tumbling angle $\langle\theta\rangle = 0.02 \pm 0.01\ \pi$, which is consistent with the physical interpretation that the RBC makes full rotations as it tumbles.

State diagram

In Fig. 2 (A and B) , the state diagrams of the time-averaged doublet fraction $\overline{\Phi}$ in the (*Ca*, ϕ) phase space shows that doublets are more likely to emerge at larger ϕ and smaller *Ca*. The highest $\overline{\Phi}$ for the suspension system occurs for $\phi > 0.045$ and $0.075 < Ca < 0.1$, and the probability of the doublet formation noticeably reduces as *Ca* becomes greater than 0.1 (Fig. 2A). $\overline{\Phi}$ rises as ϕ increases for all *Ca*. We note that the configurational snapshots and the pair correlation functions in Fig. 1C show regularly spaced RBC singlets at $\phi = 0.01$. As ϕ increases, the long-range interparticle hydrodynamic interactions promote additional RBCs to the regular positions of the RBC singlets, thus forming pairs. Thus, the doublet fraction increases as ϕ increases. In contrast, $\overline{\Phi}$ generally drops with increasing *Ca* as shown in Fig. 2A. Figure 2B shows that the doublet structure nearly vanishes for $Ca < 0.05$ in the two-cell system regardless of the volume fraction. Inasmuch as there are only two cells, there cannot be inter- and intralayer organization, and the microstructure is distinctly dissimilar from that of the suspension. Thus, the mechanism in which additional cells are promoted to regularly spaced singlet RBC positions is not available in the two-cell model. Accordingly, the discrepancy in the state diagrams between the suspension and the two-cell system could be anticipated.

Suspension viscosity

To investigate the contribution of suspending substances to the viscosity of a suspension, we calculate both the relative viscosity $\eta_{rel} = \eta / \eta_0$ and the intrinsic viscosity $[\eta] = (\eta - \eta_0)/(\eta_0 \phi) = \sigma^p_{yx}/(\dot{\gamma}\,\eta_0\,\phi)$, where η_0 is the solvent viscosity and σ^p_{yx} represents the shear component of the particle stress. Details of fluid stress and viscosity evaluations are given in Methods. For a hard sphere suspension in an unbounded domain, $[\eta] = 5/2$, and it increases with ϕ for nondilute suspensions due to increased interparticle interaction. Correspondingly, Fig. 2C shows that $[\eta]$ increases with the doublet fraction. While this is consistent with other studies of aggregating RBCs with inter-RBC attractive interactions (*50*, *51*), hydrodynamic interaction is the sole driver for the observed RBC doublet structure in this study.

Figure 3A shows that η_{rel} decreases and exhibits shear thinning as *Ca* increases for $\phi = 0.024$ to 0.06. The thinning rate $\partial\eta_{rel}/\partial Ca$ increases as ϕ increases. For $\phi < 0.04$, $\partial\eta_{rel}/\partial Ca$ is nearly invariant as *Ca* increases. This is likely due to flow-induced particle cross-stream migration, with all particles focused in the flow center plane. For $\phi > 0.04$, we observe a slight upturn in η_{rel} at the smallest *Ca*. This may be attributed to the breakup of RBC pairs or RBC clusters that occur at the higher ϕ due to the increased likelihood of interparticle collisions. The shear thinning effect is commonly observed in blood and is partially attributed to cell deformation and cell migration away from the walls, resulting in a more concentrated RBC distribution near the center.

Furthermore, synchronized rotating RBCs due to hydrodynamic interactions may also affect lower viscosity by coordinating flow around the pair (*26*, *27*). Figure 3B shows the same trends for the two-cell system, although the data variances are larger because of the smaller sample size. As expected, η_{rel} increases linearly as ϕ increases in the dilute suspension as we observe in Fig. 3 (C and D). We also observe that the slope $\partial\eta_{rel}/\partial\phi$ decreases as *Ca* increases.

Figure 4A shows that $[\eta]$ slightly increases, while ϕ increases for $Ca = 0.03$, which correlates with the increasing $\overline{\Phi}$. Figure 4A shows that $\partial[\eta]/\partial\phi \approx 0$ for $Ca = 0.06$. This may be attributed to the faster decreasing $[\eta]$ because of increasing *Ca* (and particle deformation) as ϕ increases, resulting in a crossing point at $Ca = 0.06$ as shown in Fig. 4B. Furthermore, $[\eta]$ decreases as ϕ increases and $\partial[\eta]/\partial\phi$ becomes negative for $0.08 < Ca < 0.2$. This change in $\partial[\eta]/\partial\phi$ as *Ca* increases is due to a combination of factors that affect $[\eta]$, including the interparticle arrangements, particle deformation, and also possibly the gradual transition of modes of RBC motion as *Ca* increases (*52*, *53*).

More insights may be gained by examining how $[\eta]$ depends on *Ca*. Figure 4B shows that $[\eta]$ decreases as *Ca* increases for all ϕ, which has been observed in other studies and previously attributed to RBC deformation (*52*, *53*). We observe that flow-induced microstructural reorganization also contributes to the change in $[\eta]$. Moreover, $|\partial[\eta]/\partial Ca|$ increases as ϕ increases. We observe in Fig. 2A that the change in $\overline{\Phi}$ with *Ca* is much slower for $\phi < 0.04$ compared to $\phi > 0.045$. This is also reflected in the number of nearest neighbors N_n, which is weakly dependent on *Ca* for $\phi < 0.04$ but decreases substantially as *Ca* increases for $\phi > 0.045$, as shown in Fig. 1F. Figure 2C shows that Φ is linearly correlated with $[\eta]$. These observations indicate that the

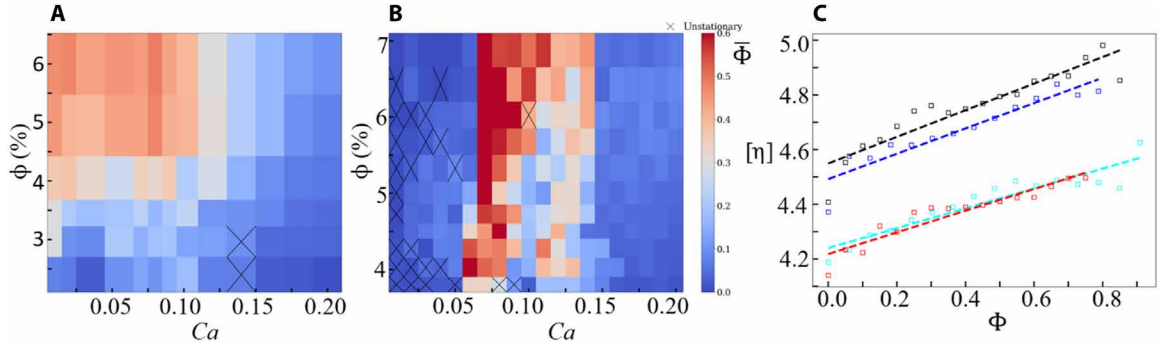

Fig. 2. Doublet dynamic state dependence in the RBC suspension. Doublet fraction state diagrams for (**A**) the RBC suspension and (**B**) the two-cell system. The color map represents the magnitude of $\overline{\Phi}$. The crosses indicate states that are found to not reach stationarity within the trial run time (see note S2 and fig. S6). (**C**) The averaged intrinsic viscosity dependence on the doublet fraction for $\phi = 0.049$, $Ca = 0.03$ (blue) and 0.06 (cyan) and $\phi = 0.06$, $Ca = 0.03$ (black) and 0.06 (red). The dashed lines are linear fits through the data.

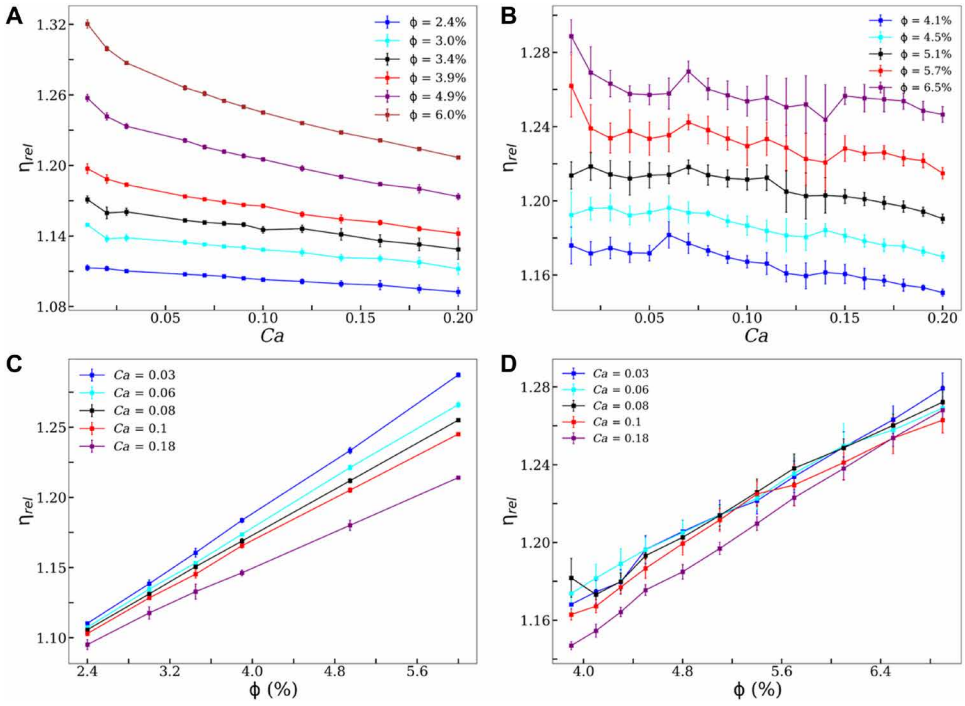

Fig. 3. Dependence of the relative viscosity on the RBC suspension properties. Relative viscosity (η_{rel}) dependence on *Ca* in (**A**) the suspension and (**B**) the two-cell system. The dependence of η_{rel} on ϕ in (**C**) the suspension and (**D**) the two-cell system.

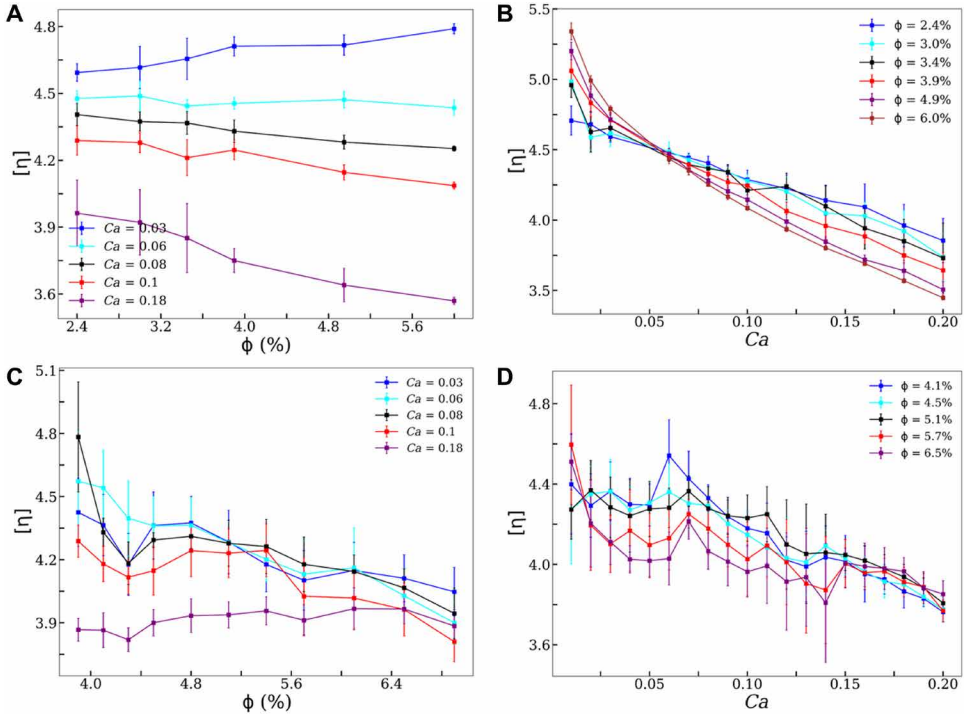

Fig. 4. Dependence of the intrinsic viscosity for the RBC suspensions. On (**A**) ϕ and (**B**) *Ca* and for the two-cell system on (**C**) ϕ and (**D**) *Ca*.

Table 1. Parameters matched to real RBC values in Système International units.

Parameters	Physical values
L	7.82×10^{-6} m
x_0	1/2.2
G	4.81×10^{-6} N/m
k_b	3×10^{-19} J
k_{ag}	2.41×10^{-4} J
k_v	2.48×10^{2} J
Y	18.9×10^{-6} N/m
ε	k_BT (T = 300 K)
r_0	0.4 μm

breakup of waltzing doublets is correlated to the change in $\partial[\eta]/\partial Ca$ with ϕ.

We also pinpoint how doublet formation influences [η] by comparison to the two-cell system. In the two-cell system, doublets do not form for $Ca < 0.05$ due to the lack of regularly spaced layers. Figure 4D shows that [η] decreases as Ca increases for all ϕ, but no curve crossing is observed for ϕ = 0.04 to 0.065. Furthermore, Fig. 4C shows $\partial[\eta]/\partial\phi < 0$ for all Ca, in contrast to the suspension system. This suggests that hydrodynamics-induced interparticle ordering is also responsible for the changes in the rheological properties of the suspension and the two-cell system.

DISCUSSION

We carry out 3D simulations of dilute suspensions of model nonadhesive RBCs in confined simple shear flow via the lattice Boltzmann method combined with the immersed boundary method to investigate flow-induced collective microstructure and associated changes to the suspension dynamic properties. In the dilute suspension, we find the emergence of intermittent synchronously rotating RBC doublets at low Ca. We observe tumbling cells align and form files along the flow direction once the hydrodynamic interaction is strong enough to drive slightly deformed cells to migrate toward the center plane of the channel. The flow field generated by particle-flow interactions result in regular spacing between RBCs in a file (*8*, *27*). RBCs in different files rotate in a synchronized manner, and more cells form pairs, revolve, and break up as though they are waltzing. As the shear stress further increases, we find that the number of files often reduces and that cells stay in more crowded bands leading to frequent collision.

Our calculations of the intrinsic viscosity reflect these microstructure transitions. At low Ca, [η] weakly increases as ϕ increases, corresponding to increased doublet fraction. At intermediate Ca, [η] is nearly independent of ϕ, which could be attributed to flow-induced ordering of RBCs. Our data also suggest that the variation of the RBC doublet fraction with respect to ϕ and Ca correlates with how [η] varies with ϕ and Ca. As Ca further increases, the RBC files may merge into wide bands. Cells repeatedly collide. Thus, disordered cell arrangements emerge and correspond to decreasing [η].

Our study shows that interparticle hydrodynamics interactions (HI) is a key factor in flow-induced microstructural arrangements of RBCs. Without including RBC-specific interactions, our results are likely applicable to other soft discoids in confined flow. However, we only examine highly confined capillaries for dilute volume fractions that correspond to specific physiological flows in microvessels. We expect that, at higher volume fractions in larger vessels, the flow-induced microstructural evolution of large RBC rouleaux becomes the key contributor to complex rheological response such as shear thinning. Our future investigations will examine how including more rigid cells (white blood cells) and smaller cells (platelets) would affect the HI-induced collective structure and dynamics.

METHODS

Fluid solver and RBC model

We apply the lattice Boltzmann method coupled with the immersed boundary method to solve this suspension flow (*42*). RBCs are confined in a channel with a height of around 1.5 L, where L is the RBC's diameter. Simple shear flow in the x direction is induced by two parallel moving walls along the y axis. We apply periodic boundary conditions in both the x and z directions. The model setup is shown in the schematic in Fig. 1A.

We closely follow a coarse-grained elastic spring network model to simulate the RBC membrane (*54*). For simplicity, the fluid viscosities inside and outside the cell are the same in this study. The biconcave shape of an RBC is parameterized by

$$y = \pm L\sqrt{1 - \frac{4(x^2 + z^2)}{L^2}}\left[a_0 + a_1\frac{x^2 + z^2}{L^2} + a_2\frac{(x^2 + z^2)^2}{L^4}\right] \quad (1)$$

where L = 7.82 μm, a typical RBC diameter. The coefficients are $a_0 = 0.0581$, $a_1 = 2.0026$, and $a_2 = -4.491$. A spring network of 642 nodes and 1280 triangular faces is used to discretize the cell membrane. To capture the in-plane elasticity of the RBC membrane, we model each spring of the network by the worm-like chain (WLC) model combined with a repulsive potential given by

$$U_{\text{in-plane}} = \sum_{j=1}^{N_s}\left[\frac{k_B T l_m(3x_j^2 - 2x_j^3)}{4p(1 - x_j)} + \frac{k_p}{l_j}\right] \quad (2)$$

where p is the persistent length, k_BT/p is the entropic force that determines the WLC strength; l_j is the length of j-th spring, $l_m \equiv l_0/x_0$ is the allowed maximum spring length determined by the parameter x_0, l_0 is the initial length of each spring, $x_j = l_j/l_m$; and k_p is the spring constant of the repulsive power potential. The discretized bending energy of the cell membrane can be written as (*54*)

$$U_{\text{out-of-plane}} = \sum_{j=1}^{N_s} k_b[1 - \cos(\theta_j - \theta_0)] \quad (3)$$

where k_b is the bending constant, θ_j is the instantaneous dihedral angle between two adjacent triangular membrane patches, and θ_0 corresponds to the spontaneous curvature of the membrane, which is defined by the initial biconcave shape. Because the lipid bilayer is nearly incompressible, we enforce membrane area conservation by applying a harmonic potential defined as

$$U_{\text{area}} = k_{ag}\frac{(A - A_t)^2}{2A_t} \quad (4)$$

where k_{ag} is the strength of the area constraint and A_t and A are the initial and instantaneous total membrane area, respectively. A volume constraint given by

$$U_{\text{volume}} = k_v \frac{(V - V_0)^2}{2V_0} \quad (5)$$

is also used to prevent a drift in the cell volume, where k_v is the constraint strength, V_0 denotes the initial RBC volume, and V is the instantaneous cell volume. To prevent particles from interpenetration, a short-range repulsive force is commonly applied to particles. The Lenard-Jones potential with a cutoff at the zero-force distance r_0 is used in this study

$$U_{\text{WCA}} = 4\varepsilon \left[\left(\frac{\sigma}{r}\right)^{12} - \left(\frac{\sigma}{r}\right)^{6} \right] \text{ for } r \leq r_0 \quad (6)$$

where ε is the potential strength, r is the distance between two membrane nodes that are on different RBCs, and $\sigma = 2^{1/6} r_0$.

The shear (G), area compression (K), and Young's (Y) moduli can be estimated from the RBC model parameters as given by

$$G = \frac{\sqrt{3}\, k_B T}{4 p l_m x_0} \left(\frac{x_0}{2(1 - x_0)^3} - \frac{1}{4(1 - x_0)^2} + \frac{1}{4} \right) + \frac{3\sqrt{3}\, k_p}{4 l_0^3} \quad (7)$$

$$K = 2G + k_{ag} \quad (8)$$

$$Y = \frac{4KG}{K + G} \quad (9)$$

The parameter values for this study are listed in Table 1.

Fluid stress and viscosity

We estimate the averaged shear stress $<\sigma_{yx}>$ by the momentum exchange between the fluid and the wall (*55*, *56*). By means of the simple bounce-back boundary condition, one can easily compute $\langle \sigma_{yx} \rangle = \sum_k \Delta p_x^k / (\Delta t A_k)$, where the area of a unit wall patch $A_k = (\Delta x)^2$, of which Δx is the lattice spacing, Δt is the integration time step, and the momentum exchange is denoted by Δp_x^k. The suspension viscosity η then can be obtained by $\eta = \langle \sigma_{yx} \rangle / \dot{\gamma}$. To look into the relationship between the suspension viscosity and the particle dynamics, we also calculate the intrinsic viscosity, defined as $[\eta] = (\eta - \eta_0)/(\eta_0 \phi) = \langle \sigma_{yx}^p \rangle / (\dot{\gamma} \eta_0 \phi)$, where η_0 is the ambient fluid viscosity and σ_{yx}^p denotes the particle stress. Chosen time trajectories of fluid stress and viscosity are provided in the Supplementary Materials.

SUPPLEMENTARY MATERIALS

Supplementary material for this article is available at https://science.org/doi/10.1126/sciadv.abq5248

REFERENCES AND NOTES

1. W. B. Russel, D. A. Saville, W. R. Schowalter, *Colloidal Dispersions* (Cambridge Univ. Press, 1991).
2. V. N. Manoharan, Colloidal matter: Packing, geometry, and entropy. *Science* **349**, 1253751 (2015).
3. M. Driscoll, B. Delmotte, Leveraging collective effects in externally driven colloidal suspensions: Experiments and simulations. *Curr. Opin. Colloid Interface Sci.* **40**, 42–57 (2019).
4. A. Snezhko, Complex collective dynamics of active torque-driven colloids at interfaces. *Curr. Opin. Colloid Interface Sci.* **21**, 65–75 (2016).
5. O. Aouane, A. Farutin, M. Thiebaud, A. Benyoussef, C. Wagner, C. Misbah, Hydrodynamic pairing of soft particles in a confined flow. *Phys. Rev. Fluids* **2**, 063102 (2017).
6. C. Iss, D. Midou, A. Moreau, D. Held, A. Charrier, S. Mendez, A. Viallat, E. Helfer, Self-organization of red blood cell suspensions under confined 2D flows. *Soft Matter* **15**, 2971–2980 (2019).
7. Z. Shen, T. M. Fischer, A. Farutin, P. M. Vlahovska, J. Harting, C. Misbah, Blood crystal: Emergent order of red blood cells under wall-confined shear flow. *Phys. Rev. Lett.* **120**, 268102 (2018).
8. S. Singha, A. R. Malipeddi, M. Zurita-Gotor, K. Sarkar, K. Shen, M. Loewenberg, K. B. Migler, J. Blawzdziewicz, Mechanisms of spontaneous chain formation and subsequent microstructural evolution in shear-driven strongly confined drop monolayers. *Soft Matter* **15**, 4873–4889 (2019).
9. A. Zöttl, H. Stark, Emergent behavior in active colloids. *J. Phys. Condens. Matter* **28**, 253001 (2016).
10. W. Fornari, L. Brandt, P. Chaudhuri, C. U. Lopez, D. Mitra, F. Picano, Rheology of confined non-Brownian suspensions. *Phys. Rev. Lett.* **116**, 018301 (2016).
11. S. Gallier, E. Lemaire, L. Lobry, F. Peters, Effect of confinement in wall-bounded non-colloidal suspensions. *J. Fluid Mech.* **799**, 100–127 (2016).
12. M. Ramaswamy, N. Y. C. Lin, B. D. Leahy, C. Ness, A. M. Fiore, J. W. Swan, I. Cohen, How confinement-induced structures alter the contribution of hydrodynamic and short-ranged repulsion forces to the viscosity of colloidal suspensions. *Phys. Rev. X* **7**, 041005 (2017).
13. C.-T. Liao, Y.-F. Wu, W. Chien, J.-R. Huang, Y.-L. Chen, Modeling shear-induced particle ordering and deformation in a dense soft particle suspension. *J. Phys. Condens. Matter* **29**, 435101 (2017).
14. S. Razavi Bazaz, A. Mashhadian, A. Ehsani, S. C. Saha, T. Krüger, M. E. Warkiani, Computational inertial microfluidics: A review. *Lab Chip* **20**, 1023–1048 (2020).
15. Z. Varga, V. Grenard, S. Pecorario, N. Taberlet, V. Dolique, S. Manneville, T. Divoux, G. H. McKinley, J. W. Swan, Hydrodynamics control shear-induced pattern formation in attractive suspensions. *Proc. Natl. Acad. Sci. U.S.A.* **116**, 12193–12198 (2019).
16. S. O. Catarino, R. O. Rodrigues, D. Pinho, J. M. Miranda, G. Minas, R. Lima, Blood cells separation and sorting techniques of passive microfluidic devices: From fabrication to applications. *Micromachines* **10**, 593 (2019).
17. S. Suresh, J. Spatz, J. P. Mills, A. Micoulet, M. Dao, C. T. Lim, M. Beil, T. Seufferlein, Connections between single-cell biomechanics and human disease states: Gastrointestinal cancer and malaria. *Acta Biomater.* **1**, 15–30 (2005).
18. M. Jaiswal, R. Dudhe, P. K. Sharma, Nanoemulsion: An advanced mode of drug delivery system. *3 Biotech* **5**, 123–127 (2015).
19. R. Fahraeus, The influence of the rouleau formation of the erythrocytes on the rheology of the blood. *Acta Med. Scand.* **161**, 151–165 (1958).
20. S. Chien, S. Usami, R. J. Dellenback, M. I. Gregersen, L. B. Nanninga, M. M. Guest, Blood viscosity: Influence of erythrocyte aggregation. *Science* **157**, 829–831 (1967).
21. H. H. Lipowsky, Microvascular rheology and hemodynamics. *Microcirculation* **12**, 5–15 (2005).
22. W. Reinke, P. Gaehtgens, P. C. Johnson, Blood viscosity in small tubes: Effect of shear rate, aggregation, and sedimentation. *Am. J. Physiol.* **253**, H540–H547 (1987).
23. C.-T. Liao, Y.-L. Chen, Shear-induced non-monotonic viscosity dependence for model red blood cell suspensions in microvessels. *Biomicrofluidics* **13**, 064115 (2019).
24. Y.-F. Wu, P.-S. Hsu, C.-S. Tsai, P.-C. Pan, Y.-L. Chen, Significantly increased low shear rate viscosity, blood elastic modulus, and RBC aggregation in adults following cardiac surgery. *Sci. Rep.* **8**, 7173 (2018).
25. J. Mauer, S. Mendez, L. Lanotte, F. Nicoud, M. Abkarian, G. Gompper, D. A. Fedosov, Flow-induced transitions of red blood cell shapes under shear. *Phys. Rev. Lett.* **121**, 118103 (2018).
26. M. Thiébaud, Z. Shen, J. Harting, C. Misbah, Prediction of anomalous blood viscosity in confined shear flow. *Phys. Rev. Lett.* **112**, 238304 (2014).
27. Z. Shen, A. Farutin, M. Thiébaud, C. Misbah, Interaction and rheology of vesicle suspensions in confined shear flow. *Phys. Rev. Fluids* **2**, 103101 (2017).
28. J. L. McWhirter, H. Noguchi, G. Gompper, Ordering and arrangement of deformed red blood cells in flow through microcapillaries. *New J. Phys.* **14**, 085026 (2012).
29. A. Karnis, S. G. Mason, Particle motions in sheared suspensions: XXIII. Wall migration of fluid drops. *J. Colloid Interface Sci.* **24**, 164–169 (1967).
30. P. C.-H. Chan, L. G. Leal, An experimental study of drop migration in shear flow between concentric cylinders. *Int. J. Multiph. Flow* **7**, 83–99 (1981).
31. J. R. Smart, D. T. Leighton Jr., Measurement of the drift of a droplet due to the presence of a plane. *Phys. Fluids A* **3**, 21–28 (1991).
32. M. R. Kennedy, C. Pozrikidis, R. Skalak, Motion and deformation of liquid drops, and the rheology of dilute emulsions in simple shear flow. *Comput. Fluids* **23**, 251–278 (1994).
33. S. K. Doddi, P. Bagchi, Lateral migration of a capsule in a plane Poiseuille flow in a channel. *Int. J. Multiph. Flow* **34**, 966–986 (2008).
34. C. W. Hsu, Y.-L. Chen, Microflow fractionation of deformable particles. *J. Chem. Phys.* **133**, 034906 (2010).
35. H. Zhao, A. P. Spann, E. S. G. Shaqfeh, The dynamics of a vesicle in a wall-bound shear flow. *Phys. Fluids* **23**, 121901 (2011).
36. S. C. Hur, N. K. Henderson-MacLennan, E. R. McCabe, D. Di Carlo, Deformability-based cell classification and enrichment using inertial microfluidics. *Lab Chip* **11**, 912–920 (2011).
37. H. Mohammadigoushki, J. J. Feng, Size-differentiated lateral migration of bubbles in Couette flow of two-dimensional foam. *Phys. Rev. Lett.* **109**, 084502 (2012).

38. A. Kumar, M. D. Graham, Mechanism of margination in confined flows of blood and other multicomponent suspensions. *Phys. Rev. Lett.* **109**, 108102 (2012).
39. Y.-L. Chen, Inertia- and deformation-driven migration of a soft particle in confined shear and Poiseuille flow. *RSC Adv.* **4**, 17908 (2014).
40. M. Abkarian, A. Viallat, Dynamics of vesicles in a wall-bounded shear flow. *Biophys. J.* **89**, 1055–1066 (2005).
41. D. A. Fedosov, B. Caswell, A. S. Popel, G. E. Karniadakis, Blood flow and cell-free layer in microvessels. *Microcirculation* **17**, 615–628 (2010).
42. T. Krüger, F. Varnik, D. Raabe, Efficient and accurate simulations of deformable particles immersed in a fluid using a combined immersed boundary lattice Boltzmann finite element method. *Comput. Math. Appl.* **61**, 3485–3505 (2011).
43. S. Ishida, R. Matsumoto, D. Matsunaga, Y. Imai, Particle segregation using crystal-like structure of capsules in wall-bounded shear flow. *Phys. Rev. Fluids* **7**, 063601 (2022).
44. H. L. Goldsmith, J. Marlow, F. C. MacIntosh, Flow behaviour of erythrocytes - I. Rotation and deformation in dilute suspensions. *Proc. R. Soc. B* **182**, 351–384 (1972).
45. S. Ramanujan, C. Pozrikidis, Deformation of liquid capsules enclosed by elastic membranes in simple shear flow: Large deformations and the effect of fluid viscosities. *J. Fluid Mech.* **361**, 117–143 (1998).
46. H. Noguchi, Swinging and synchronized rotations of red blood cells in simple shear flow. *Phys. Rev. E* **80**, 021902 (2009).
47. K. Sinha, M. D. Graham, Dynamics of a single red blood cell in simple shear flow. *Phys. Rev. E* **92**, 042710 (2015).
48. G. B. Jeffery, The motion of ellipsoidal particles immersed in a viscous fluid. *Proc. R. Soc. A* **102**, 161–179 (1922).
49. A. Z. Yazdani, R. M. Kalluri, P. Bagchi, Tank-treading and tumbling frequencies of capsules and red blood cells. *Phys. Rev. E* **83**, 046305 (2011).
50. B. Quaife, S. Veerapaneni, Y.-N. Young, Hydrodynamics and rheology of a vesicle doublet suspension. *Phys. Rev. Fluids* **4**, 103601 (2019).
51. M. Abbasi, A. Farutin, H. Ez-Zahraouy, A. Benyoussef, C. Misbah, Erythrocyte-erythrocyte aggregation dynamics under shear flow. *Phys. Rev. Fluids* **6**, 023602 (2021).
52. N. Takeishi, M. E. Rosti, Y. Imai, S. Wada, L. Brandt, Hemorheology in dilute, semi-dilute and dense suspensions of red blood cells. *J. Fluid Mech.* **872**, 818–848 (2019).
53. A. N. Ouhra, A. Farutin, O. Aouane, H. Ez-Zahraouy, A. Benyoussef, C. Misbah, Shear thinning and shear thickening of a confined suspension of vesicles. *Phys. Rev. E* **97**, 012404 (2018).
54. D. A. Fedosov, B. Caswell, G. E. Karniadakis, Systematic coarse-graining of spectrin-level red blood cell models. *Comput. Methods Appl. Mech. Eng.* **199**, (2010).
55. A. J. C. Ladd, Numerical simulations of particulate suspensions via a discretized Boltzmann equation. Part 1. Theoretical foundation. *J. Fluid Mech.* **271**, 285–309 (1994).
56. M. Gross, T. Krüger, F. Varnik, Rheology of dense suspensions of elastic capsules: Normal stresses, yield stress, jamming and confinement effects. *Soft Matter* **10**, 4360–4372 (2014).

Acknowledgments: We thank insightful discussions with F.-W. Wang, C.-C. Hsieh, C.-F. Chou, J.-R, Huang, and C.-K. Chan. We thank the computing resources provided by Academia Sinica TWGrid Computing Center and National Center for High-Performance Computing, Taiwan. **Funding:** This work was funded by the Ministry of Science and Technology grant MOST 110-2112-M-001-067-MY3 and Academia Sinica Grand Challenges Seed grant AS-GSC-111-M02. **Author contributions:** Conceptualization: C.-T.L., A.-J.L., and Y.-L.C. Methodology: C.-T.L., A.-J.L., and Y.-L.C. Investigation: C.-T.L. and A.-J.L. Visualization: C.-T.L. and A.-J.L. Supervision: Y.-L.C. Writing—original draft: C.-T.L., A.-J.L., and Y.-L.C. Writing—review and editing: C.-T.L., A.-J.L., and Y.-L.C. **Competing interests:** The authors declare that they have no competing interests. **Data and materials availability:** All data needed to evaluate the conclusions in the paper are present in the paper and/or the Supplementary Materials.

Submitted 13 April 2022
Accepted 11 October 2022
Published 25 November 2022
10.1126/sciadv.abq5248